Nanoscale

PAPER

View Article Online
View Journal | View Issue

Cite this: *Nanoscale*, 2016, **8**, 17887

Water bridge coordination on the metal-rich facets of Gd_2O_3 nanoplates confers high T_1 relaxivity†

Zijian Zhou,[a,b] Rong Hu,[a] Lirong Wang,[a] Chengjie Sun,[a] Gang Fu[a] and Jinhao Gao*[a]

Received 15th August 2016,
Accepted 22nd September 2016

DOI: 10.1039/c6nr06444b

www.rsc.org/nanoscale

The realization of the nature of water coordination on the solid surfaces may provoke an essential understanding of T_1 relaxation enhancement, especially in nanoparticulate systems. We report herein that the T_1 relaxivity of Gd_2O_3 nanoplates is highly dependent on water coordinating behaviors on different surfaces. Gd_2O_3 nanoplates with metal-rich {100} facets showed an approximately 4-fold higher r_1 value compared to that with oxygen-terminated {111} facets. Density functional theory (DFT) calculations show that the enhanced T_1 relaxivity of Gd_2O_3 {100} nanoplates may be ascribed to the high density of accessible Gd^{3+}, fast exchange of water, and more importantly, multicenter (one-to-two) coordination for water molecules with magnetic centers on the metal-rich surface.

Introduction

The rise of two-dimensional (2D) nanomaterials has provoked invaluable opportunities for scientists to investigate structure–property relationships in solid state nanochemistry.[1–4] Due to the intriguing electronic and physical properties caused by morphological confinement effects, these 2D nanomaterials have shown unprecedented performance in electronics,[3,5] catalysis,[6–8] energy storage,[9,10] and nanomedicine.[11–13] The classical Solomon–Bloembergen–Morgan (SBM) theory for magnetic resonance imaging (MRI) contrast agents indicates that T_1 relaxation of protons is related to their chemical exchange efficiency in paramagnetic molecular systems.[14,15] However, there is still a major gap to bridge the T_1 relaxivity and water interacting behaviors in nanoparticulate systems. We have recently recognized that iron oxide nanoplates with metal-rich exposed facets showed enhanced T_1 relaxivity, probably due to the more favorable water coordination and chemical exchange on such surfaces compared to spherical nanoparticles.[16,17] One major concern for iron oxide nanoplates is, however, that they are superparamagnetic, and thus the T_1 relaxation enhancement efficiency may be blurrily disturbed by the strong T_2 decaying effect.[18,19] A suitable model to reveal the relationship between the surface structure and the T_1 relaxivity of magnetic nanoparticles is highly desirable, which would arouse great research interest in innovating the design considerations for high-performance MRI contrast agents.[20–25]

Traditional theoretic models were established on molecular systems, which only focused on the case that one water molecule (for systems with $q = 1$) interacts with one paramagnetic metal ion (denoted as one-to-one coordination hereafter).[26–28] For magnetic nanomaterials, however, the packed crystal structure may allow one water molecule to interact with two or more paramagnetic metal ions in their vicinity (multicenter coordination).[29] Moreover, a specific surface would permit the fast exchange of water molecules on magnetic centers, thus holding great potential to enhance the T_1 relaxivity. Fortunately, advanced synthetic methodologies allow us to achieve the controlled synthesis of nanomaterials with different surface features.[30,31] We propose here that the metal-rich surface of magnetic nanomaterials could allow water bridging coordination with two magnetic centers (Fig. 1a). Therefore, it is conceivable that the spin-lattice relaxation effects between water molecules and magnetic centers would be significantly enhanced compared with that of the one-to-one situation, which may confer the efficient recovery of proton longitudinal magnetizations within one relaxation time slot (Fig. 1b). Owing to the low magnetic susceptibility and diminished T_2 interference at room temperature, paramagnetic gadolinium oxide (Gd_2O_3) nanoparticles have shown great promise in T_1 contrast imaging.[32,33] Ultrasmall Gd_2O_3 nano-

[a]*State Key Laboratory of Physical Chemistry of Solid Surfaces, The MOE Key Laboratory of Spectrochemical Analysis & Instrumentation, and The Key Laboratory for Chemical Biology of Fujian Province, College of Chemistry and Chemical Engineering, Xiamen University, Xiamen 361005, P. R. China.*
E-mail: jhgao@xmu.edu.cn
[b]*Laboratory of Molecular Imaging and Nanomedicine, National Institute of Biomedical Imaging and Bioengineering, National Institutes of Health, Bethesda, MD 20892, USA*

†Electronic supplementary information (ESI) available: Experimental details, additional TEM images, *M–H* and *M–T* data, DLS data, biocompatibility study and DFT calculations and models. See DOI: 10.1039/c6nr06444b

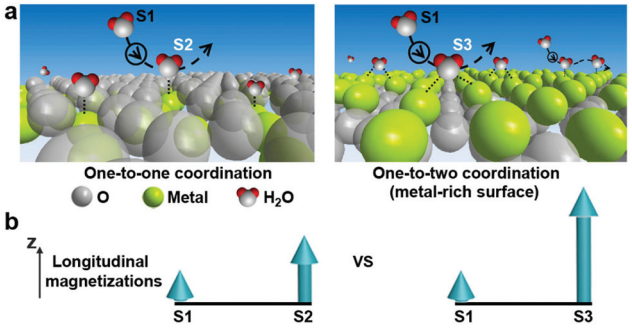

Fig. 1 Different phenomena proposed for water coordination on magnetic crystals with different surfaces. (a) Metal-rich surface may permit one-to-two coordination for water, in contrast to traditional one-to-one coordination. (b) Proposed recovery of longitudinal magnetizations for protons with different water coordinating behaviors on solid surfaces.

particles and nanoplates have been reported to show high T_1 relaxivity.[34–36] However, the relationship between the surface structure and the T_1 relaxivity of Gd_2O_3 nanoparticles has rarely been investigated.

Herein, we present the successful controlled synthesis of Gd_2O_3 nanoplates with two types of surface exposure, $Gd_2O_3\{100\}$ and $Gd_2O_3\{111\}$ facets, respectively. The $Gd_2O_3\{100\}$ facet is exposed with gadolinium ions at the outermost layer, while the $Gd_2O_3\{111\}$ facet is terminated by oxygen ions. We illustrated that the metal-rich exposed $Gd_2O_3\{100\}$ facet plays a decisive role in the enhanced T_1 relaxivity, showing approximately 4-fold higher r_1 values than that of $Gd_2O_3\{111\}$ nanoplates at different magnetic fields (0.5, 1.5, and 3.0 T). Density functional theory (DFT) calculation confirmed that the water molecule coordinating on the $Gd_2O_3\{100\}$ facet requires a lower energy than that on the $Gd_2O_3\{111\}$ facet, indicating a higher coordination efficiency on the $Gd_2O_3\{100\}$ nanoplates. More importantly, the DFT results also suggested that water hopping and re-coordination on the $Gd_2O_3\{100\}$ facet require very low transition state energy (0.08 and 0.13 eV, respectively), indicating a distinct mechanism for studying the chemical exchange of water molecules on Gd_2O_3 nanoplates.

Results and discussion

We used gadolinium(III) acetate as the precursor to synthesize Gd_2O_3 nanoplates with {100} facets as the exposed surfaces. A transmission electron microscopy (TEM) image showed that the side length and width are about 120 and 40 nm, respectively (Fig. 2a). A high-resolution TEM (HRTEM) image of a flat nanoplate showed a pair of perpendicularly crossed lattices with a spacing distance of 2.7 Å, which can be matched to the (400) plane of the cubic Gd_2O_3 phase (Fig. 2b). The in-plane fast Fourier transformation (FFT) pattern suggested the [100] zone axis (Fig. 2b, inset). Additionally, the HRTEM image of a perpendicular nanoplate showed interplanar distances of

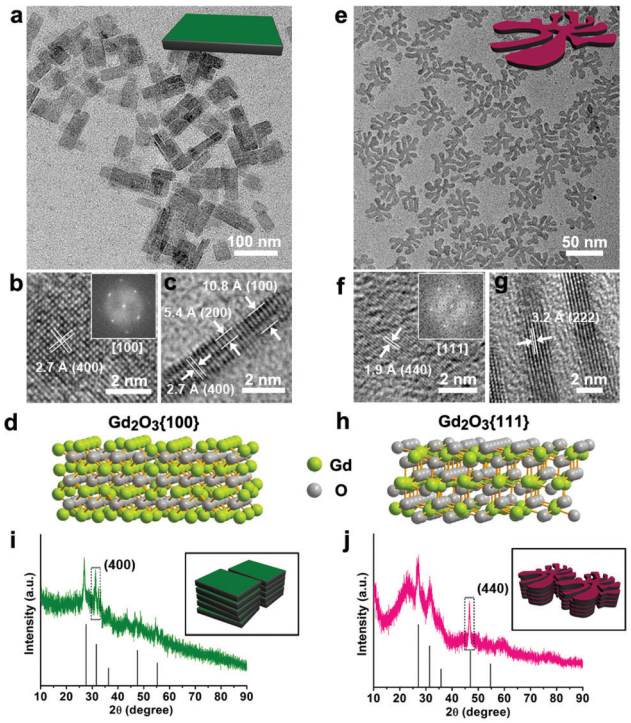

Fig. 2 TEM and HRTEM images of (a–c) $Gd_2O_3\{100\}$ and (e–g) $Gd_2O_3\{111\}$ nanoplates. The interplanar distances of 2.7, 5.4, 10.8, 1.9, and 3.2 Å are assigned to the (400), (200), (100), (440), and (220) planes of the cubic Gd_2O_3 phase, respectively. The insets show the cartoon models (a, e) and FFT patterns (b, f) corresponding to two nanoplates, respectively. Crystal structure side views of (d) $Gd_2O_3\{100\}$ and (h) $Gd_2O_3\{111\}$ facets. (i, j) XRD patterns indicate an enhanced diffraction peak for (400) and (440) planes, corresponding to the Lamer assembled $Gd_2O_3\{100\}$ and $Gd_2O_3\{111\}$ nanoplates, respectively.

2.7, 5.4, and 10.8 Å corresponding to the (400), (200), and (100) planes of the cubic Gd_2O_3 phase, respectively, indicating that the obtained Gd_2O_3 nanoplates (named $Gd_2O_3\{100\}$ square nanoplates) are only one unit cell in thickness (Fig. 2c). It is worth noting that the $Gd_2O_3\{100\}$ facet is a metal-rich surface terminated by gadolinium ions (Fig. 2d and S1†). We can also tune the length and width of the Gd_2O_3 nanoplates by controlling the molar ratio of the surfactant to the precursor (Fig. S2†). The synthesis of $Gd_2O_3\{111\}$ nanoplates using gadolinium oleate as the precursor showed a dendritic morphology in the in-plane direction (named $Gd_2O_3\{111\}$ dendritic nanoplates) with an edge length of about 65 nm (Fig. 2e). The HRTEM image of a flat plate exhibited a lattice spacing distance of 1.9 Å corresponding to the (440) plane of the cubic Gd_2O_3 phase. The in-plane FFT pattern indicated the [111] zone axis (Fig. 2f and inset). The HRTEM image of perpendicular plates further showed the (222) plane with a spacing distance of 3.2 Å (Fig. 2g). Altogether, it is concluded that the obtained nanoplates are exposed with the $Gd_2O_3\{111\}$ facet on the surfaces. In contrast, the $Gd_2O_3\{111\}$ facet is terminated by oxygen ions rather than gadolinium ions (Fig. 2h and S1†). The role of sodium oleate during the formation of $Gd_2O_3\{111\}$

nanoplates is likely to serve as both facet controlling agents in the early stage of nucleation and particle coalescence molecules during the later stage of growth of the Gd_2O_3{111} nanoplates (Fig. S3†).[37,38]

We then used X-ray diffraction (XRD) patterns to identify the crystalline phase of these two Gd_2O_3 nanoplates. Both Gd_2O_3{100} and Gd_2O_3{111} nanoplates showed a typical cubic phase (JCPDS: 012-0797) rather than a monoclinic structure, which are consistent with those derived from the HRTEM images and FFT patterns. Interestingly, the XRD pattern of the Gd_2O_3{100} nanoplates showed an enhanced diffraction peak at 33.2 degrees corresponding to the (400) planes, probably due to the face-by-face Lamer assembly structure on the substrate for XRD measurements (Fig. 2i and inset).[39] Likewise, the Gd_2O_3{111} nanoplates showed an enhanced diffraction peak at 47.5 degrees corresponding to the (440) planes in the XRD pattern (Fig. 2j and inset). These results further confirmed that both Gd_2O_3{100} and Gd_2O_3{111} nanoplates are dominated with an ultrathin plate structure. The X-ray photoelectron spectroscopy (XPS) analysis of the Gd_2O_3 nanoplates revealed two distinctive peaks at binding energies of 142.6 and 1187.3 eV coresponding to Gd 4d and Gd 3d5 transitions, respectively (Fig. S4†).

The hysteresis curves indicated that both Gd_2O_3{100} and Gd_2O_3{111} nanoplates are paramagnetic at 300 K (Fig. 3a). The unsaturated magnetic moments reached 3.4 and 4.4 emu g^{-1} for the Gd_2O_3{100} and Gd_2O_3{111} nanoplates under a magnetic field of 5 T at 300 K, respectively, indicating typical paramagnetism. When measured at a low temperature of 5 K, the nearly saturated magnetization (M_s) values of the Gd_2O_3{100} and Gd_2O_3{111} nanoplates are about 88.9 and 96.3 emu g^{-1}, respectively (Fig. 3b). It is interesting that the Gd_2O_3{100} nanoplates showed a slight tendency to be saturated at a high field range (3–5 kOe) at low temperatures, indicating a phase transition on such ultrathin nanoplates. This phenomenon was also observed at the hysteresis curves of other ultrathin Gd_2O_3 nanoplates (Fig. S5†). The typical paramagnetism of the obtained Gd_2O_3 nanoplates has also been evidenced by the thermal dependent zero field cooling (ZFC) and field cooling (FC) curves (Fig. S6†).

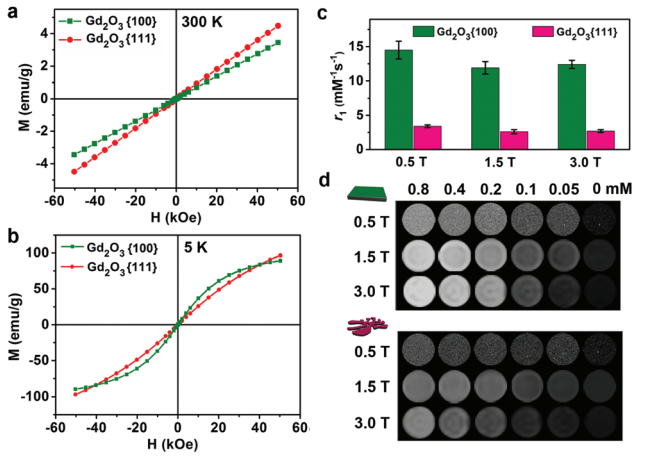

Fig. 3 (a, b) Magnetic hysteresis (M–H) loops of Gd_2O_3{100} and Gd_2O_3{111} nanoplates at 300 and 5 K. (c) Bar chart shows the T_1 relaxivity for the two nanoplates at 0.5, 1.5, and 3.0 T. (d) MR phantom study of the two nanoplates at 0.5, 1.5, and 3.0 T. Concentrations correspond to Gd^{3+} ions.

We used sodium citrate as a surface modifier to endow Gd_2O_3 nanoplates with thin-layer coating on the surface and make them water-soluble (Fig. S7†), which is in principle extremely important for studying their intrinsic T_1 relaxivity.[16,17] The T_1 contrast performance of the Gd_2O_3 nanoplates was evaluated at three different magnetic fields (0.5, 1.5, and 3.0 T). The Gd_2O_3{111} nanoplates showed relatively low r_1 values of 3.4, 2.6, and 2.7 mM^{-1} s^{-1} at 0.5, 1.5, and 3.0 T, respectively (Fig. 3c). For the Gd_2O_3{100} nanoplates, these r_1 values are 14.5, 11.9, and 12.4 mM^{-1} s^{-1} at 0.5, 1.5, and 3.0 T, respectively, which are approximately 4-fold higher than those of the Gd_2O_3{111} nanoplates. Consequently, an MR phantom study of the Gd_2O_3{100} nanoplates showed an excellent T_1 contrast with clearly brighter signals as the metal concentration was increased (Fig. 3d). In contrast, the Gd_2O_3{111} nanoplates showed a weak T_1 contrast due to the low T_1 relaxivity under the same conditions.

DFT study has received increasingly broad applications for interpreting and predicting complex behaviors at the atomic scale in chemical and materials sciences, for example water splitting on the surface of nanoparticles.[40,41] Proton T_1 relaxation is highly dependent on the coordination and chemical exchange of water molecules on the surfaces when nanoparticles were employed. The thermodynamic phenomena and kinetic behaviors between water molecules and magnetic centers are of great importance in T_1 contrast efficiency. Therefore, we investigated the water interacting behaviors with crystal surfaces by means of DFT calculation.

The Gd_2O_3{111} facet is terminated with oxygen ions, while Gd^{3+} ions are at the second outermost layer. The Gd_2O_3{111} facet accommodates 16 surface Gd^{3+} ions in one unit cell, 4 of which are six-coordinated and inaccessible for water (Fig. 4a, top view, and Fig. S8†). The remaining 12 Gd^{3+} ions are in five-coordinated configuration, which still have vacancy to coordinate with one water molecule. DFT calculations indicated that the coordinated water molecules can be in the dissociated molecular form. As shown in Fig. 4a, 5 of 12 five-coordinated Gd^{3+} ions (pink dashed circle) could induce the dissociation of H_2O into two –OH groups with the assistance of nearby oxygen atoms, yielding an average adsorption energy of −1.32 eV. On the other hand, water molecules would be weakly adsorbed on the top sites of the other 7 Gd^{3+} ions with an average adsorption energy of −0.75 eV (Fig. 4a, black dashed circle). The high stability for dissociated water indicated extremely low exchange efficiency such that the dissociated water only acts as a 'spectator' during the relaxation process. Thus, the density of the exchangeable water on the {111} facet can be estimated to be ~3.4 per nm^2 (Fig. S9†).

For the Gd_2O_3{100} facet, there are 8 three-coordinated Gd^{3+} ions in one unit cell, resulting in 8 top sites, 16 bridge

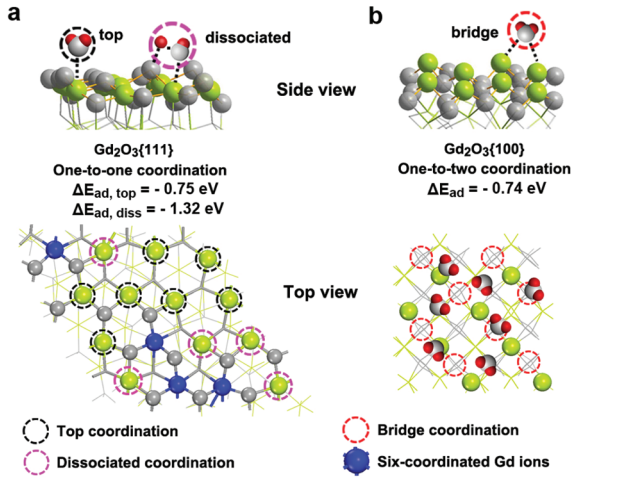

Fig. 4 Water coordinating behaviors on (a) Gd_2O_3{111} and (b) Gd_2O_3{100} facets (upper: side view, lower: top view) according to DFT calculations. Blue balls represent Gd^{3+} ions with saturated six-coordinated configuration. Black and pink dashed circles represent one-to-one top coordination and dissociated coordination for water molecules on the Gd_2O_3{111} facet, respectively. The red dashed circle represents one-to-two bridge coordination for water molecules on the Gd_2O_3{100} facet.

sites and 8 hollow sites (Fig. S10†). We found that all these sites are able to be coordinated with water molecules, and the surface is able to accommodate at most 8 water molecules (Fig. 4b, red dashed circle). Test calculations demonstrated that more water addition would lead to multilayer adsorption. For simplicity, we assumed that 8 water molecules occupied the same type sites. According to DFT calculations, the average adsorption energies for the top site, bridge site and hollow site were predicted to be −0.80, −0.74, and −0.81 eV, respectively, indicating that all water molecules on the {100} facet could be highly exchangeable (Fig. S10†). An ideal way to compare the relaxivity difference of the Gd_2O_3{100} and Gd_2O_3{111} facets is the corresponding nanoplates with the same size and morphology. However, the facets exposed on a nanocrystal have a strong correlation with the shape. The Gd_2O_3 crystal of the cubic phase tends to form Gd_2O_3{100} and Gd_2O_3{111} nanoplates with cubic and spherical shapes due to the anisotropic crystal growth under controllable conditions. Thus, so far it has been difficult to obtain Gd_2O_3 nanoplates with the same morphology but with different exposed facets. In this respect, we carefully calculated the densities of water coordination on the Gd_2O_3{100} and Gd_2O_3{111} facets. The density of water coordination on the Gd_2O_3{100} facet was estimated to be ~6.8 per nm^2, nearly twice that on the Gd_2O_3{111} facet (Fig. S9†). Thus, the higher density of exchangeable water on Gd_2O_3{100} may offer part of the explanation for the observed higher r_1 values than that of Gd_2O_3{111}. In addition, we disclosed that, besides the one-to-one coordinate mode (top site), there is one-to-two mode on bridge and hollow sites (note that the water molecules on the hollow sites deviated from the central position), resulting in two short and two long Gd–O bonds. Such new coordinated modes would promote spin-lattice relaxation effects between protons and nearby Gd^{3+} ions, which in turn increases the T_1 relaxivity. More significantly, nearly degenerate energies of water coordination on Gd_2O_3{100} suggested that the potential energy surface was very smooth, thus facilitating the fast migration of water from one magnetic center to another.

We further explored the possible migration process of water molecules on the Gd_2O_3{100} facets (Fig. 5a). DFT calculations demonstrated that water migration from one top site to another through a bridging-mediated process was calculated with transition energy barriers as low as 0.08 and 0.13 eV for two transition states TS1 and TS2, respectively, indicating great potential for water dissociation and re-coordination from one Gd^{3+} ion to another Gd^{3+} ion in vicinity (Fig. 5b).[42,43] As reported previously,[44,45] T_1 relaxivity is not only related to the coordination status but also much dependent on the kinetic exchange of water molecules on magnetic centers (Fig. 5c and d). Our findings indicated that the Gd_2O_3{100} facet not only provides rich and multicenter sites for water coordination, but also facilitates the migration of water molecules among the magnetic centers, thus enhancing the T_1 relaxivity.

Prior to conducting an *in vivo* study, we first evaluated the potential toxicity of the Gd_2O_3 nanoplates at the cellular level and in living animals. The MTT (3-(4,5-dimethylthiazol-2-yl)-2,5-diphenyl-tetrazolium bromide) assay showed that more than 95% of both HeLa and SMMC-7721 cells were viable after being treated with Gd_2O_3{100} and Gd_2O_3{111} nanoplates for 24 h even with a maximum concentration (with respect to Gd ions) up to 10 μM, indicating good biocompatibility *in vitro* (Fig. S11†). The histological study further revealed that no organ abnormalities or lesions were found in mice (n = 3)

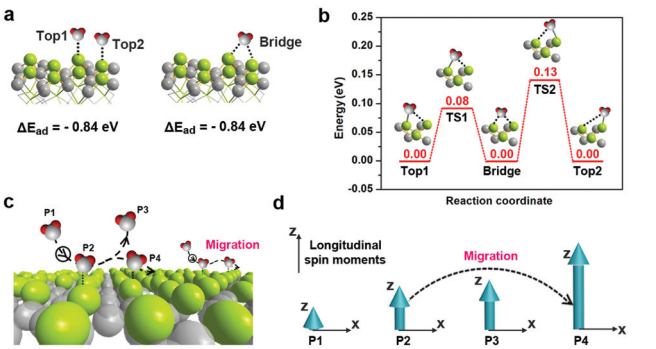

Fig. 5 Water migration on the metal-rich exposed Gd_2O_3{100} facet. (a, b) Simulation and calculated energies for one water molecule migrating from Top1 to Top2 through the bridge-mediated configuration on the Gd_2O_3{100} facet, showing the transition energy barriers as low as 0.08 eV (TS1) and 0.13 eV (TS2). (c) The water coordination and dissociation from position 1 (P1) to P2 and P3, or migration and re-coordination from P2 to P4 during the time slot of T_1 relaxation. (d) P1 to P2 and P3 are considered with moderate recovery for longitudinal magnetizations, while the migration immediately after the dissociation from P2 and re-coordination on P4 may promise cascade recovery of proton longitudinal magnetizations during the time slot of T_1 relaxation.

treated with either Gd_2O_3{100} or Gd_2O_3{111} nanoplates (2.0 mg [Gd] per kg mouse body weight) for 24 h, as indicated by the histology of the major organs of the liver, kidney, muscle, heart, lung, and spleen (Fig. S12†). The toxicity of Gd-based agents is mainly related to the release of free Gd^{3+} ions. Our *in vitro* and *in vivo* results show that both Gd_2O_3{100} and Gd_2O_3{111} nanoplates are nontoxic in the treatment period of 24 h, suggesting little to no release of free Gd^{3+} ions from Gd_2O_3 nanoplates during this period. The long-term biosafety study should be conducted in future. For *in vivo* imaging study, we injected either Gd_2O_3{100} or Gd_2O_3{111} nanoplates in mice through a tail vein with a dose of 2.0 mg [Gd] per kg mouse body weight. The T_1 MRI contrast performance was evaluated at a 3.0 T clinical scanner both at coronal and transverse planes at the region of interest (ROI) of the liver, due to the fact that circulating nanoparticles are prone to be accumulated in the liver by a mononuclear phagocyte system (MPS).[46–48] The contrast-enhanced MRI results showed an obviously brighter signal at the liver region after 0.5 h post-injection (p.i.) of Gd_2O_3{100} nanoplates, which continuously increased over time to 2 h p.i. (Fig. 6a). After that, a decreased liver signal was found at 4 h p.i., the reason for which might be multifold: either the excretion of nanoplates from the liver or stacking of nanoplates in the liver will cause the loss of T_1 signal.[17] On the contrary, the Gd_2O_3{111} nanoplates exhibited little to no contrast in T_1 MRI at the ROI under similar conditions (Fig. 6b). We used the ΔSNR (signal-to-noise ratio, $\Delta SNR = |SNR_{post} - SNR_{pre}|/SNR_{pre}$) to quantify the T_1 signal changes in the ROI.[46] The results implied that the ΔSNR at the ROI treated with Gd_2O_3{100} nanoplates are 2–4 fold higher than those being treated with Gd_2O_3{111} nanoplates at different time points (Fig. 6c and d). These results are consistent with the MR phantom study, further indicating the superior T_1 relaxation enhancement of the Gd_2O_3{100} nanoplates both *in vitro* and *in vivo*.

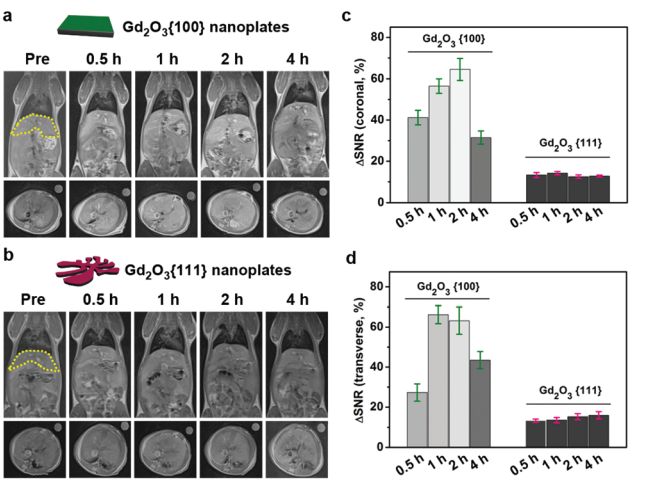

Fig. 6 (a, b) T_1 MRI study in a mouse model injected with Gd_2O_3{100} and Gd_2O_3{111} nanoplates in a dose of 2.0 mg [Gd] per kg mouse body weight. The pre-injection and 0.5, 1, 2, and 4 h post-injection images at coronal (top) and transverse (bottom) planes were acquired focusing the ROI of the liver (yellow dotted circle as shown in the first image). The upper right circles at each of transverse images indicate water. (c, d) Comparison of the quantitative signal changes ΔSNR (signal-to-noise ratio) at the ROI after injection with Gd_2O_3{100} and Gd_2O_3{111} nanoplates at the coronal and transverse planes, respectively.

Conclusions

In conclusion, we report that gadolinium oxide nanoplates with metal-rich Gd_2O_3{100} exposed facets exhibited significantly enhanced T_1 contrast ability, compared to that with oxygen terminated Gd_2O_3{111} facets. The enhanced T_1 relaxivity of the Gd_2O_3{100} nanoplates can be attributed to the following factors: (i) the higher density of water coordination due to the large number of exposed Gd^{3+} ions on the Gd_2O_3{100} nanoplates; (ii) the one-to-two coordinated configurations of water coordination on the metal-rich exposed Gd_2O_3{100} facets permit significantly enhanced spin-lattice relaxation effects; (iii) the smooth potential energy surface for water coordination enables bridge-mediated fast migration among different magnetic sites, thus facilitating cascade recovery of longitudinal magnetizations. The present work by integrating the experimental results with theoretical simulation may not only provoke an essential understanding of T_1 relaxation enhancement effects in nanoparticulate systems, but also shed light on the innovations of T_1 contrast agents for high-performance MRI applications.

Experimental

Materials and characterization

1-Octadecene (ODE, tech. 90%) and oleic acid (tech. 90%) were purchased from Acros. Gadolinium(III) chloride hexahydrate (99.99%) and gadolinium acetate (99.9%) were purchased from Alfa Aesar. Sodium oleate, sodium citrate, iron chlorides and other reagents are purchased from Sinopharm Chemical Reagent Co. Ltd. All chemicals were used as received without further purification. TEM and HRTEM images were recorded on a JEM-2100 microscope at an accelerating voltage of 200 kV. X-ray diffraction (XRD) patterns were recorded by using a Rigaku Ultima IV X-ray diffractometer with Cu Kα radiation. X-ray photoelectron spectroscopy (XPS) measurements were carried out by using a PHI Quantum-2000 photoelectron spectrometer. The hysteresis loops (at 300 K and 5 K) and temperature-dependent magnetization measurements were recorded on a Quantum Design MPMS-XL-7 system. The elemental analysis of metal ions was performed by inductively coupled plasma atomic emission spectroscopy (ICP-AES). The dynamic light scattering measurements were performed on a Malvern Zetasizer nano ZS instrument. The MRI measurements and T_2/T_1 relaxation time testing were performed on a 0.5 T NMI20-Analyst NMR analyzing & imaging system (Niumag Corporation, Shanghai, China) and a 3.0 T imaging system (Philips Medical System, ACHIEVA 3.0 T).

Synthesis of Gd_2O_3{111} nanoplates

The gadolinium oleate complex was synthesized as a precursor through a general procedure reported elsewhere (ref. 16). We synthesized {111} facets exposed Gd_2O_3 nanoplates by decomposition of the gadolinium oleate complex in the presence of oleic acid and sodium oleate. 1-Octadecene (ODE) was used as a solvent with a boiling temperature at 314 °C. The addition of sodium oleate leads to the formation of circular, triangular, and dendritic shaped nanoplates by controlling the molar ratio to the gadolinium oleate precursor. For example, 1 mmol (1.0 g) of the gadolinium oleate complex was dissolved in 15 mL of ODE in the presence of 160 μL of oleic acid. 0.5 mmol (151 mg) of sodium oleate was added to the solution and the system was heated to reflux under an N_2 atmosphere. The reaction was then ceased by removing the heating source after a 2 h reflux and allowed to cool to room temperature. The dendritic Gd_2O_3 nanoplates were obtained by centrifugation and washed with hexane and ethanol solution three times. The formation of circular and triangular shaped Gd_2O_3 nanoplates was carried out by a similar procedure but with the addition of 0.1 mmol (30 mg) and 0.2 mmol (60 mg) of sodium oleate, respectively. The final product was redispersed in hexane and stored at 4 °C for further use.

Synthesis of Gd_2O_3{100} nanoplates

The synthesis of Gd_2O_3{100} nanoplates is followed by the decomposition of the gadolinium(III) acetate precursor in the presence of oleic acid in the solvent of ODE. For example, 0.334 g (1 mmol) of gadolinium acetate were dissolved in 10 mL of ODE solvent with the addition of 0.34 mL (1 mmol) of oleic acid. The system was degassed with nitrogen and heated to reflux with a constant heating rate of ~8 °C min^{-1}. The reaction was then ceased and allowed to cool to room temperature after 2 h reflux. After the addition of an excess of isopropanol, a white product was obtained through centrifugation. The product was redispersed in hexane and stored at 4 °C for further use. The side length and the width of the Gd_2O_3{100} nanoplates can be controlled by tuning the molar ratio of the precursor to surfactant. The Gd_2O_3{100} nanoplates with a side length and width of 120 × 40 nm and 90 × 15 nm were obtained with the precursor to surfactant molar ratio of 1 : 1 and 1 : 2, respectively.

Preparation of water-soluble Gd_2O_3 nanoplates

The preparation of sodium citrate coated Gd_2O_3 nanoplates was carried out in a straightforward manner as follows: an excess of sodium citrate (10 mg) was dissolved in a flask containing 5 mL of ultra-pure water and 10 mL of tetrahydrofuran, and then the as-prepared hexane-dispersed Gd_2O_3 nanoplates (0.1 mmol) were added to the flask. The solution was then heated to reflux for 2 h before the nanoparticles were transferred to the lower layer. The solution in the lower layer was then collected and centrifuged at 8000 rpm to obtain the precipitate. The final product was redispersed in distilled water (or PBS) and stored at 4 °C for further use.

MR relaxivity and MR phantom study

The Gd_2O_3 nanoplates with various gadolinium metal concentrations were prepared within 1% agar for MR phantom study. The relaxivity and phantom studies of the Gd_2O_3 nanoplates were conducted at three different magnetic fields (0.5, 1.5, and 3.0 T). The longitudinal (r_1) and transverse (r_2) relaxivities of the Gd_2O_3 nanoplates were obtained from the slopes of the reciprocal of each relaxation time against concentration. T_2- and T_1-weighted MR images were acquired with the following parameters: TR/TE = 2000/60 ms (T_2), TR/TE = 300/10 ms (T_1), 128 × 128 matrices, and repetition time = 8.

Density functional theory (DFT) calculations

All the calculations were performed with the density functional theory (DFT) provided by the Vienna *ab initio* simulation package (VASP). The exchange and correlation were treated with the generalized gradient approximation (GGA) *via* the Perdew–Burke–Ernzerhof (PBE) function. The $5s^25p^64f^75d^16s^2$ shells of the Gd and $2s^22p^4$ shells of O have been considered explicitly in the spin-polarized density functional theory (SDFT) calculations. The GGA + U approach was utilized for all calculations, where the parameters U and J were not entered into the density functional separately but considered as a combined effective interaction parameter. We used U = 7.5 eV, J = 0.6 eV in all GGA + U calculations, resulting in a U_{eff} of 6.9 eV applied to the 4f orbital of the Gd atoms. A charge density cutoff energy of 400 eV was used for the smooth part of the electronic wave functions and the augmented electron density. Brillouin zone integration was optimized at the Γ-point with a Monkhorst–Pack k-point grid of 1 × 1 × 1 for the bulk and slab model. All the atomic positions in the bulk structure were relaxed, while we fixed the bottom two layers in the slab. The convergence criteria for the energy calculation and structure optimization are set to a self-consistent field tolerance of 1.0×10^{-5} eV and a maximum Hellmann–Feynman force tolerance of 0.02 eV $Å^{-1}$. We consider the C-type cubic structure of gadolinium sesquioxide with the space group $Ia\bar{3}$. We have performed a full optimization (lattice constant and atomic position) of the bulk. The Gd-terminated {100} surface with 8 atomic layers and a vacuum region of 15 Å was employed. The O-terminated {111} surface has been modeled for a 3-atomic-layer slab with 120 atoms, and with the bottom one layer frozen. We performed antiferromagnetic ordering for the Gd magnetic moments. Water adsorption energy is calculated using the following equation: $\Delta E_{ads(H_2O)} = E_{(H_2O/surf)} - E_{(surf)} - E_{(H_2O)}$, where $E_{(H_2O)}$ is the energy of the water molecule, and $E_{(H_2O/surf)}$ and $E_{(surf)}$ refer to the energies of the chosen surface with or without water, respectively.

In vivo MRI study

Animal experiments were executed according to the protocol approved by the Institutional Animal Care and Use Committee of Xiamen University. We conducted an *in vivo* MRI study in a mouse model (~20 g, female ICR) using a clinical 3 T MRI scanner (Philips Medical System, ACHIEVA 3.0 T). The

pre-injection T_1 images of the anaesthetized mice both at the coronal and transverse planes were acquired for comparison purpose. The mice were injected with water-soluble Gd_2O_3{100} or Gd_2O_3{111} nanoplates with a dose of 2.0 mg [Gd] per kg to the mouse body weight. The post-injection (p.i.) time points of 0.5, 1, 2, and 4 h were acquired both at the coronal and transverse planes. All the T_1 images were acquired using a fast spin-echo sequence (FSE) with the following parameters: TR/TE = 300/14 ms, thickness = 1 mm, 144 × 144 matrices, FOV = 100 × 100 mm (coronal) or 50 × 50 mm (transverse), and flip angle = 90°.

Acknowledgements

This work was supported by the National Key Basic Research Program of China (2013CB933901, 2014CB744502, and 2014CB932004), the National Natural Science Foundation of China (21222106, 21521004, 81370042, and 81430041), Fok Ying Tung Education Foundation (142012), and the Intramural Research Program, National Institute of Biomedical Imaging and Bioengineering, National Institutes of Health.

References

1 Y. Sun, S. Gao, F. Lei, C. Xiao and Y. Xie, *Acc. Chem. Res.*, 2015, **48**, 3–12.
2 H. Zhang, *ACS Nano*, 2015, **9**, 9451–9469.
3 A. K. Geim and K. S. Novoselov, *Nat. Mater.*, 2007, **6**, 183–191.
4 M. A. Boles, D. Ling, T. Hyeon and D. V. Talapin, *Nat. Mater.*, 2016, **15**, 141–153.
5 D. Akinwande, N. Petrone and J. Hone, *Nat. Commun.*, 2014, **5**, 5678.
6 F. Song and X. Hu, *J. Am. Chem. Soc.*, 2014, **136**, 16481–16484.
7 K. Zhou and Y. Li, *Angew. Chem., Int. Ed.*, 2012, **51**, 602–613.
8 B. Luo, G. Liu and L. Wang, *Nanoscale*, 2016, **8**, 6904–6920.
9 M. F. El-Kady, V. Strong, S. Dubin and R. B. Kaner, *Science*, 2012, **335**, 1326–1330.
10 L. Hu, X. Wu and J. Yang, *Nanoscale*, 2016, **8**, 12939–12945.
11 Z. Liu, J. T. Robinson, X. Sun and H. Dai, *J. Am. Chem. Soc.*, 2008, **130**, 10876–10877.
12 H. Wang, X. Yang, W. Shao, S. Chen, J. Xie, X. Zhang, J. Wang and Y. Xie, *J. Am. Chem. Soc.*, 2015, **137**, 11376–11382.
13 X. Qian, S. Shen, T. Liu, L. Cheng and Z. Liu, *Nanoscale*, 2015, **7**, 6380–6387.
14 I. Solomon, *Phys. Rev.*, 1955, **99**, 559–565.
15 N. Bloembergen and L. O. Morgan, *J. Chem. Phys.*, 1961, **34**, 842–850.
16 Z. Zhou, C. Wu, H. Liu, X. Zhu, Z. Zhao, L. Wang, Y. Xu, H. Ai and J. Gao, *ACS Nano*, 2015, **9**, 3012–3022.
17 Z. Zhou, Z. H. Zhao, H. Zhang, Z. Wang, X. Chen, R. Wang, Z. Chen and J. Gao, *ACS Nano*, 2014, **8**, 7976–7985.
18 R. V. Jagadeesh, A.-E. Surkus, H. Junge, M.-M. Pohl, J. Radnik, J. Rabeah, H. Huan, V. Schünemann, A. Brückner and M. Beller, *Science*, 2013, **342**, 1073–1076.
19 J. Huang, Y. Hou, C. Liu, L. Jing, T. Ma, X. Sun and M. Gao, *Chem. Mater.*, 2015, **27**, 7918–7925.
20 N. Lee, D. Yoo, D. Ling, M. H. Cho, T. Hyeon and J. Cheon, *Chem. Rev.*, 2015, **115**, 10637–10689.
21 T.-H. Shin, Y. Choi, S. Kim and J. Cheon, *Chem. Soc. Rev.*, 2015, 4501–4516.
22 T. Todd, Z. Zhen, W. Tang, H. Chen, G. Wang, Y.-J. Chuang, K. Deaton, Z. Pan and J. Xie, *Nanoscale*, 2014, **6**, 2073–2076.
23 F. Li, D. Zhi, Y. Luo, J. Zhang, X. Nan, Y. Zhang, W. Zhou, B. Qiu, L. Wen and G. Liang, *Nanoscale*, 2016, **8**, 12826–12833.
24 L. Zhang, R. Liu, H. Peng, P. Li, Z. Xu and A. K. Whittaker, *Nanoscale*, 2016, **8**, 10491–10510.
25 R. Hachani, M. Lowdell, M. Birchall, A. Hervault, D. Mertz, S. Begin-Colin and N. T. K. Thanh, *Nanoscale*, 2016, **8**, 3278–3287.
26 R. B. Lauffer, *Chem. Rev.*, 1987, **87**, 901–927.
27 P. Caravan, C. T. Farrar, L. Frullano and R. Uppal, *Contrast Media Mol. Imaging*, 2009, **4**, 89–100.
28 P. Caravan, *Chem. Soc. Rev.*, 2006, **35**, 512–523.
29 J. Yu, L. Qi and M. Jaroniec, *J. Phys. Chem. C*, 2010, **114**, 13118–13125.
30 Y. Xia, Y. Xiong, B. Lim and S. E. Skrabalak, *Angew. Chem., Int. Ed.*, 2009, **48**, 60–103.
31 Y. Wang, J. He, C. Liu, W. H. Chong and H. Chen, *Angew. Chem., Int. Ed.*, 2015, **54**, 2022–2051.
32 J. Y. Park, M. J. Baek, E. S. Choi, S. Woo, J. H. Kim, T. J. Kim, J. C. Jung, K. S. Chae, Y. Chang and G. H. Lee, *ACS Nano*, 2009, **3**, 3663–3669.
33 J. S. Ananta, B. Godin, R. Sethi, L. Moriggi, X. Liu, R. E. Serda, R. Krishnamurthy, R. Muthupillai, R. D. Bolskar, L. Helm, M. Ferrari, L. J. Wilson and P. Decuzzi, *Nat. Nanotechnol.*, 2010, **5**, 815–821.
34 M. Cho, R. Sethi, J. S. Ananta narayanan, S. S. Lee, D. N. Benoit, N. Taheri, P. Decuzzi and V. L. Colvin, *Nanoscale*, 2014, **6**, 13637–13645.
35 H. Dong, S.-R. Du, X.-Y. Zheng, G.-M. Lyu, L.-D. Sun, L.-D. Li, P.-Z. Zhang, C. Zhang and C.-H. Yan, *Chem. Rev.*, 2015, **115**, 10725–10815.
36 T. Paik, T. R. Gordon, A. M. Prantner, H. Yun and C. B. Murray, *ACS Nano*, 2013, **7**, 2850–2859.
37 D. Wang, Y. Kang, X. Ye and C. B. Murray, *Chem. Mater.*, 2014, **26**, 6328–6332.
38 Z. Zhou, X. Zhu, D. Wu, Q. Chen, D. Huang, C. Sun, J. Xin, K. Ni and J. Gao, *Chem. Mater.*, 2015, **27**, 3505–3515.
39 X. Han, Q. Kuang, M. Jin, Z. Xie and L. Zheng, *J. Am. Chem. Soc.*, 2009, **131**, 3152–3153.
40 M. Zobel, R. B. Neder and S. A. J. Kimber, *Science*, 2015, **347**, 292–294.
41 B. Wu, H. Huang, J. Yang, N. Zheng and G. Fu, *Angew. Chem., Int. Ed.*, 2012, **51**, 3440–3443.

42 H.-F. Wang, R. Kavanagh, Y.-L. Guo, Y. Guo, G.-Z. Lu and P. Hu, *Angew. Chem., Int. Ed.*, 2012, **51**, 6657–6661.
43 X. Meng, J. Guo, J. Peng, J. Chen, Z. Wang, J.-R. Shi, X.-Z. Li, E.-G. Wang and Y. Jiang, *Nat. Phys.*, 2015, **11**, 235–239.
44 E. J. Werner, A. Datta, C. J. Jocher and K. N. Raymond, *Angew. Chem., Int. Ed.*, 2008, **47**, 8568–8580.
45 P. Caravan, J. J. Ellison, T. J. McMurry and R. B. Lauffer, *Chem. Rev.*, 1999, **99**, 2293–2352.
46 J. Huang, L. Bu, J. Xie, K. Chen, Z. Cheng, X. Li and X. Chen, *ACS Nano*, 2010, **4**, 7151–7160.
47 F. Geissmann, S. Gordon, D. A. Hume, A. M. Mowat and G. J. Randolph, *Nat. Rev. Immunol.*, 2010, **10**, 453–460.
48 A. Chow, B. D. Brown and M. Merad, *Nat. Rev. Immunol.*, 2011, **11**, 788–798.